This paper appears in Advanced Intelligent Systems, 2020.
https://doi.org/10.1002/aisy.201900181

Modeling and Emulating a Physiotherapists Role in Robot-Assisted Rehabilitation

Ran Tao, Renz Ocampo, Jason Fong, Abed Soleymani, and Mahdi Tavakoli

***Abstract*—In home-based rehabilitation, one possible approach is haptic teleoperation in which a hospital-based therapist is haptically linked and tele-presented to a home-based patient to effectively simulate traditional in-hospital therapies over a distance. In this context, this paper proposes a learn-and-replay (LAR) paradigm that consists of two phases: A therapist-in-loop (interactive) phase where the therapist interacts through the haptic teleoperation loop with the patient to perform one or more repetitions of the cooperative therapy task, and a therapist-out-of-loop (standalone) phase where the therapist's cooperative role of the task is played by the patient-side robot in future repetitions. During the interactive phase, the therapist demonstrates impedance during cooperating with the patient in performing the task. During the standalone phase, the patient-side robot is automatically controlled to mimic the therapist's demonstrated impedance which is learned in the interactive phase. The Direct Force Reflection (DFR) architecture is utilized as the control method for the bilateral telerehabilitation system. Case studies involving one degree-of-freedom and two-degree-of-freedom cooperative manipulation tasks are tested for proof of concept. In the experiment, the therapists and patients were simulated by using healthy participants (the authors of the paper) and were located in the same room to show a proof-of-concept idea of the work. The results show that the impedance of the therapist's arm can be replicated by the patient-side robot for both tasks and proposed LAR telerehabilitation paradigm assists the therapist in the rehabilitation procedure to takecare of other tasks or attend to other patients.**

***List of Acronyms* — LTI: Linear time-invariant, CNS: Central nervous system, DFR: Direct force reflection, DOF: Degree of freedom, LfD: Learning from demonstration, LAR: Learn and replay.**

I. Introduction

Due to the greater incidence of stroke on the ageing population, the demand for rehabilitation therapy for post-stroke patients has been increasing. Each patient requires many lengthy hands-on therapy sessions with rehabilitation therapists, which are labour-intensive activities and place a significant burden on the healthcare system. This demand has motivated the incorporation of robotic systems into rehabilitation programs as robots can perform controlled and reproducible motions and are not subject to fatigue. The use of robots helps to relieve the therapists from repetitive hands-on therapy exercises.

Earlier works in the field of rehabilitation robotics set a precedent for providing therapeutic interaction through impedance-based robotic interaction, where impedance is the dynamic relationship between a movement perturbation and the force generated in response to that movement perturbation [1]. Research on human physical interaction has provided evidence that humans execute manipulation tasks and interact with the outside environment by treating the interaction as an impedance-based system. Humans display task-dependent closed-loop dynamics via the incorporation of inverse dynamic models and impedance control while interacting with the environment [2, 3]. The central nervous system (CNS) learns the optimal impedance for a specific interaction and while the interaction can be intrinsically unstable, stability is achieved via regulating the mechanical impedance in the human arm [4]. The above two studies, therefore, show the relevance of implementing impedance control in robotics to provide human-like interaction, as a therapist would during conventional hand-over-hand therapy.

However, early methods of providing impedance-based interactions such as in [1] are rudimentary in that the impedances are set arbitrarily by the robot programmers. More recent approaches revolve around teaching robots biomimetic impedance interaction, such as the method based on adaptive controllers [5]. Probabilistic approaches such as learning from demonstration (LfD) have been extensively used to learn impedance-based interactions, such as through characterizing the demonstration variance [6]. LfD using gaussian mixture models has also been employed, for example, to capture the impedance pattern of two humans in haptic interaction during a hardware assembly task [7]. The impedance pattern was then reproduced by a robot for autonomous robot-human collaboration. Inspired by these approaches, our presented work will involve the learning and transfer of human arm impedance to a robotic system via teleoperation.

Bilateral teleoperation has been proposed in the past as a method by which a therapist can retain hands-on involvement in robotic rehabilitation [8, 9]. Recent efforts, provide interaction between a therapist and patient through impedance surfaces [10]. In this paper, the explored idea is to instead make the patient-side rehabilitation robot (slave robot) learn the endpoint impedance displayed by the therapist using therapist-side robot (master robot) and then emulate the therapist's behaviour for the task.

In this paper, we propose a novel paradigm called learn and replay (LAR) to realize direct bilateral telerehabilitation that encompasses two distinct phases to achieve the time-sharing of a therapist. During the first phase, the therapist interacts directly with a patient through bilateral teleoperation (Fig. 1(a)) to complete a cooperative task. This phase is called the therapist-in-loop (interactive) phase. Throughout the interaction, the therapist's task-specific impedance is measured through the therapist-side robot. During the next stage, the therapist is no longer in the rehabilitation loop, thus giving rise to the therapist-out-of-loop (standalone) phase (Fig. 1(b)). In

This research was supported by the Natural Sciences and Engineering Research Council (NSERC) of Canada under grant CRDPJ 411603, the Canada Foundation for Innovation (CFI) under grant LOF 28241, the Alberta Innovation and Advanced Education Ministry under Small Equipment Grant RCP-12-021, and Quanser Inc.

Ran Tao, Renz Ocampo, Jason Fong, Abed Soleymani, and Mahdi Tavakoli (Corresponding Author) are with the Department of Electrical and Computer Engineering, University of Alberta, Edmonton, AB T6G 2V4, Canada. E-mails: {ran1, rocampo, jmfong, zsoleymani, mahdi.tavakoli}@ualberta.ca

the standalone phase, the therapist's measured arm impedance is displayed to the patient by the patient-side robot via an impedance control loop so that the cooperative rehabilitation task can be carried out in the absence of the therapist.

The mechanical impedance of the human arm (which we aim to teach to our robotic system) is often measured via system identification methods. Either position or force perturbations are applied by a robot to the hand, and the resulting force and motion responses are analyzed to fit typically to a second-order impedance model. For example, a planar robot can be used to impose step position disturbances to the human hand, enabling the calculation of the endpoint stiffness of the arm in the Cartesian plane [11]. Later, dynamic components, i.e. damping and inertia can be added to the impedance model [12, 13, 14]. In rehabilitation, the mechanical arm impedance can potentially serve as a quantifiable index to measure patient recovery. Both position and force perturbations can be applied to the arm to identify a second-order impedance model [15]. When force perturbations are applied, the subject is required to maintain a certain posture. While this approach maximizes the model precision and consistency, it is geared toward assessing patient recovery and not therapists. It will be impractical for the interactive phase of our proposed LAR telerehabilitation paradigm, as to restrain the therapist to a certain posture during the entire session of therapy does not facilitate therapy. The endpoint impedance of the human arm can be measured in a real-world task by applying short, impulsive force perturbations to the arm during the execution of the task [16, 17, 18]. Force perturbations with 3N amplitude and 100 ms duration can be exerted on the hand holding the weld gun [18]. Segments of data immediately following the onset of perturbations with 200 ms of duration were used to identify a second-order impedance model. A modified version of this approach is implemented in this paper.

We believe that the proposed paradigm is worth researching because of the following three reasons: 1) It provides the rehabilitation robot with a desired therapy-oriented behaviors by *demonstrating* the task rather than explicitly *programming* it through machine commands. This feature is useful in clinical settings where the therapist normally doesn't have the knowledge to reprogram/reconfigure the robot. 2) It also facilitates time-sharing the same therapist across multiple home-based patients engaged in task-oriented therapy. The therapist can engage the next patient in the interactive phase while the previous patient starts standalone phase exercises. The different therapist arm impedances related to different patients and different therapy tasks will be identified and emulated by different patient-side robots. 3) Finally, the LAR paradigm is also particularly useful for sophisticated impedance-based rehabilitation tasks that are highly relevant to activities of daily living (ADL); this paradigm can also accomplish simpler trajectory-following tasks.

This paper is organized as follows: In Section II, we present a general control architecture involving up to 6 degrees-of-freedom (DOF) for LAR therapy. In Section III, we introduce the method used for human arm impedance measurement in the interactive phase without interrupting the normal flow of the therapy task. In Section IV, we present the impedance control implementation for the patient-side robot during the standalone phase. In Section V, we present two case studies involving a 1-DOF task and a 2-DOF task. Finally, Section VI presents the concluding remarks.

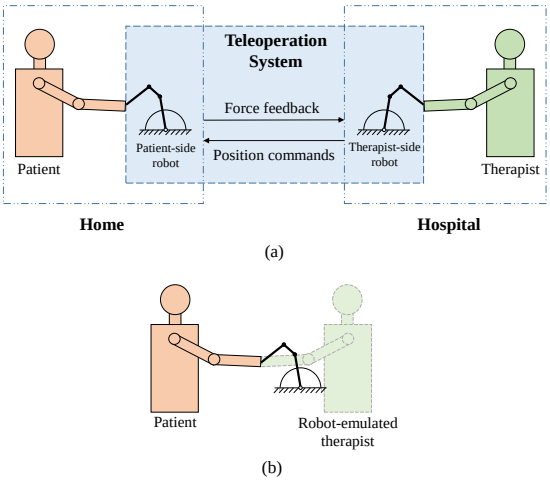

Figure 1: Illustration of the proposed LAR paradigm with (a) interactive phase, where the hospital-based therapist interacts with the home-based patient via a teleoperation system, and (b) standalone phase where the therapist's behaviour is emulated by the patient-side robot

II. Telerehabilitation System

A. *therapist-side and patient-side Robot Kinematics*

Consider a bilateral teleoperation system operating in n DOF (n up to 6), comprising of a therapist-side robot (placed on the therapist side), a patient-side robot (placed on the patient side), a communication system and a control architecture. We can denote the joint angles of the therapist-side robot with $\boldsymbol{\theta}_m = [\theta_{1m} \;\; \theta_{2m} \;\ldots\; \theta_{nm}]^T$ and the joint angles of the patient-side robot with $\boldsymbol{\theta}_s = [\theta_{1s} \;\; \theta_{2s} \;\ldots\; \theta_{ns}]^T$. The position of the end-effector of the therapist-side and patient-side robots in Cartesian space can be denoted by $\boldsymbol{p}_m$ and $\boldsymbol{p}_s$ respectively, each being a n-by-1 vector. The velocity in joint space and Cartesian space are linked by the n-by-n Jacobian matrices $\boldsymbol{J}_m$ and $\boldsymbol{J}_s$ for the therapist-side and patient-side robots:

$$\dot{\boldsymbol{p}}_m = \boldsymbol{J}_m \dot{\boldsymbol{\theta}}_m \tag{1}$$

$$\dot{\boldsymbol{p}}_s = \boldsymbol{J}_s \dot{\boldsymbol{\theta}}_s \tag{2}$$

Joint torques applied by the motors are denoted by $\boldsymbol{\tau}_m = [\tau_{1m} \;\; \tau_{2m} \;\ldots\; \tau_{nm}]^T$ for the therapist-side robot and $\boldsymbol{\tau}_s = [\tau_{1s} \;\; \tau_{2s} \;\ldots\; \tau_{ns}]^T$ for the patient-side robot. We can therefore relate static joint torques to the end-effector Cartesian forces, $\boldsymbol{f}_m$ for the therapist-side robot and $\boldsymbol{f}_s$ for the patient-side robot, by

$$\boldsymbol{\tau}_m = \boldsymbol{J}_m^T \boldsymbol{f}_m \tag{3}$$

$$\boldsymbol{\tau}_s = \boldsymbol{J}_s^T \boldsymbol{f}_s \tag{4}$$

Similarly, Cartesian forces applied by human operators onto the robots, $\boldsymbol{f}_{th}$ for the forces applied to the therapist-side robot by the therapist and $\boldsymbol{f}_p$ for the forces applied to the patient-side robot by the patient, can be mapped to their

corresponding joint torques $\boldsymbol{\tau}_{th} = [\tau_{th1} \;\; \tau_{th2} \; ... \; \tau_{thn}]^T$ and $\boldsymbol{\tau}_p = [\tau_{p1} \;\; \tau_{p2} \; ... \; \tau_{pn}]^T$ by

$$\boldsymbol{\tau}_{th} = \boldsymbol{J}_m^T \boldsymbol{f}_{th} \tag{5}$$

$$\boldsymbol{\tau}_p = \boldsymbol{J}_s^T \boldsymbol{f}_p \tag{6}$$

B. therapist-side and patient-side Robot Dynamics

Both the therapist-side and the patient-side robots can be modeled with the following motion equations. The therapist-side robot dynamics can be modeled by

$$\boldsymbol{M}_m(\boldsymbol{\theta}_m)\ddot{\boldsymbol{\theta}}_m + \boldsymbol{N}_m(\boldsymbol{\theta}_m, \dot{\boldsymbol{\theta}}_m) + \boldsymbol{f}_{rm}(\boldsymbol{\theta}_m, \dot{\boldsymbol{\theta}}_m) - \boldsymbol{\tau}_{th} = \boldsymbol{\tau}_m \tag{7}$$

where

$$\boldsymbol{N}_m(\boldsymbol{\theta}_m, \dot{\boldsymbol{\theta}}_m) = \boldsymbol{C}_m(\boldsymbol{\theta}_m, \dot{\boldsymbol{\theta}}_m)\dot{\boldsymbol{\theta}}_m + \boldsymbol{G}_m(\boldsymbol{\theta}_m) \tag{8}$$

and $\boldsymbol{M_m}$ denotes the inertia matrix for the therapist-side robot, $\boldsymbol{C}_m$ denotes the Coriolis and centrifugal matrix, $\boldsymbol{G}_m$ denotes the therapist-side robot's gravity vector and $\boldsymbol{f}_{rm}$ denotes the joint friction torque vector. $\boldsymbol{\tau}_{th}$ is preceded by a negative sign because in this paper, we decide to consider forces/torques applied by the robot to be positive, and that the forces/torques applied by the environment to the robot to be negative. This choice is arbitrary.

The patient-side robot dynamics can be modeled by

$$\boldsymbol{M}_s(\boldsymbol{\theta}_s)\ddot{\boldsymbol{\theta}}_s + \boldsymbol{N}_s(\boldsymbol{\theta}_s, \dot{\boldsymbol{\theta}}_s) + \boldsymbol{f}_{rs}(\boldsymbol{\theta}_s, \dot{\boldsymbol{\theta}}_s) - \boldsymbol{\tau}_p = \boldsymbol{\tau}_s \tag{9}$$

where

$$\boldsymbol{N}_s(\boldsymbol{\theta}_s, \dot{\boldsymbol{\theta}}_s) = \boldsymbol{C}_s(\boldsymbol{\theta}_s, \dot{\boldsymbol{\theta}}_s)\dot{\boldsymbol{\theta}}_s + \boldsymbol{G}_s(\boldsymbol{\theta}_s) \tag{10}$$

and $\boldsymbol{M}_s$ denotes the inertia matrix for the patient-side robot, $\boldsymbol{C}_s$ denotes the patient-side robot's Coriolis and centrifugal matrix, $\boldsymbol{G}_s$ denotes the patient-side robot's gravity vector and $\boldsymbol{f}_{rs}$ denotes the joint friction torque vector.

C. Telerehabilitation System Controller

A direct force reflection (DFR) architecture will be used for control of the bilateral telerehabilitation system. In the DFR architecture, the patient-side robot follows the position of the therapist-side robot while the therapist-side robot displays to the human operator the interaction forces measured by a force sensor at the patient-side robot's end-effector. This architecture achieves perfect force tracking and assumes that the environment is modeled by a linear spring. For further details of this teleoperation control method, readers can refer to [19]. A detailed schematic of the bilateral teleoperation system is presented in Fig. 2. Note that uppercase letters are used to denote the Laplace transforms of the corresponding time-domain position, velocity, force and torque variables.

The matrix $\boldsymbol{Q}$ is introduced to transform the therapist-side robot joint angles into reference joint angles for the corresponding patient-side joints. $\boldsymbol{K}_s$ refers to the PD position

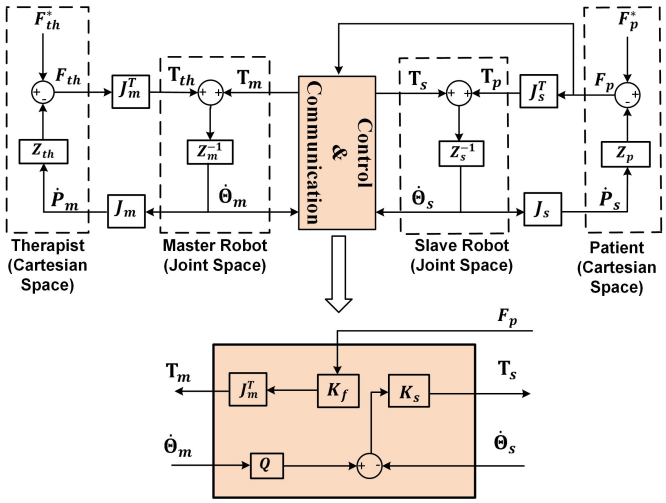

Figure 2: Schematic of the teleoperation control architecture

controller for the patient-side robot:

$$\boldsymbol{K}_s = \begin{bmatrix} K_{v1} + \dfrac{K_{p1}}{s} & 0 & \cdots & 0 \\ 0 & K_{v2} + \dfrac{K_{p2}}{s} & \cdots & 0 \\ \vdots & \vdots & \ddots & \vdots \\ 0 & 0 & \cdots & K_{vn} + \dfrac{K_{pn}}{s} \end{bmatrix} \tag{11}$$

Note that the inputs to the controller matrix $\boldsymbol{K}_s$ are velocities, not positions, as shown later in (18).

$\boldsymbol{K}_f$ refers to the force feedback gain matrix for the therapist-side robot:

$$\boldsymbol{K}_f = \begin{bmatrix} K_{f1} & 0 & \cdots & 0 \\ 0 & K_{f2} & \cdots & 0 \\ \vdots & \vdots & \ddots & \vdots \\ 0 & 0 & \cdots & K_{fn} \end{bmatrix} \tag{12}$$

$\boldsymbol{Z}_m$ and $\boldsymbol{Z}_s$ denote the linear impedance matrices in the joint domain of the therapist-side and patient-side robot that we approximate from the nonlinear robot dynamics. $\boldsymbol{Z}_{th}$ and $\boldsymbol{Z}_p$ refer to the impedance matrices in the Cartesian domain of the therapist's arm and the patient's arm respectively. As can be seen in Fig. 2, the teleoperation system is divided into five subsystems: therapist, therapist-side robot, control & communication, patient-side robot and patient. For the therapist and patient, we have

$$\boldsymbol{F}_{th} = \boldsymbol{F}_{th}^* - \boldsymbol{Z}_{th}\dot{\boldsymbol{P}}_m \tag{13}$$

$$\boldsymbol{F}_p = \boldsymbol{F}_p^* - \boldsymbol{Z}_p\dot{\boldsymbol{P}}_p \tag{14}$$

where $\boldsymbol{F}_{th}^*$ and $\boldsymbol{F}_p^*$ denote the therapist's and patient's input forces (generated by the muscles with command sent from the central nervous system). For the therapist-side robot and the patient-side robot we have

$$\boldsymbol{T}_{th} + \boldsymbol{T}_m = \boldsymbol{Z}_m\dot{\boldsymbol{\Theta}}_m \tag{15}$$

$$\boldsymbol{T}_p + \boldsymbol{T}_s = \boldsymbol{Z}_s\dot{\boldsymbol{\theta}}_s \tag{16}$$

As the therapist and patient work in Cartesian space but the

robots work in joint spaces, Jacobian matrices are needed as interfaces between the therapist and therapist-side robot, as well as between the patient and the patient-side robot, to convert Cartesian forces to joint domain torques (based on (5) and (6)) and to convert joint velocities to Cartesian velocities (based on (1) and (2)). As for the controller, we have

$$\boldsymbol{T}_m = \boldsymbol{J}_m^T \boldsymbol{K}_f \boldsymbol{F}_p \tag{17}$$

for the force feedback control on the therapist-side robot, and

$$\boldsymbol{T}_s = \boldsymbol{K}_s(\boldsymbol{Q}\dot{\boldsymbol{\Theta}}_m - \dot{\boldsymbol{\theta}}_s) \tag{18}$$

for the patient-side robot's position control.

By combining (15), (16), (17) and (18), the overall system dynamics in the frequency domain can be derived:

$$\boldsymbol{J}_m \boldsymbol{Z}_m^{-1} \boldsymbol{J}_m^T (\boldsymbol{F}_{th} + \boldsymbol{K}_f \boldsymbol{F}_p) = \dot{\boldsymbol{P}}_m \tag{19}$$

$$\boldsymbol{J}_s \boldsymbol{Z}_s^{-1} (\boldsymbol{J}_s^T \boldsymbol{F}_p + \boldsymbol{K}_s (\boldsymbol{Q}\boldsymbol{J}_m^{-1}\dot{\boldsymbol{P}}_m - \boldsymbol{J}_s^{-1}\dot{\boldsymbol{P}}_s)) = \dot{\boldsymbol{P}}_s \tag{20}$$

Equations (19) and (20) can be manipulated into the following 2-port network hybrid matrix form

$$\begin{bmatrix} \boldsymbol{F}_{th} \\ -\dot{\boldsymbol{P}}_s \end{bmatrix} = \begin{bmatrix} \boldsymbol{H}_{11} & \boldsymbol{H}_{12} \\ \boldsymbol{H}_{21} & \boldsymbol{H}_{22} \end{bmatrix} \begin{bmatrix} \dot{\boldsymbol{P}}_m \\ \boldsymbol{F}_p \end{bmatrix} \tag{21}$$

where

$$\boldsymbol{H}_{11} = \boldsymbol{J}_m^{-T} \boldsymbol{Z}_m \boldsymbol{J}_m^{-1} \tag{22}$$

$$\boldsymbol{H}_{12} = -\boldsymbol{K}_f \tag{23}$$

$$\boldsymbol{H}_{21} = -(\boldsymbol{J}_s \boldsymbol{Z}_s^{-1} \boldsymbol{K}_s \boldsymbol{J}_s^{-1} + \boldsymbol{I}_{n\times n})^{-1} \boldsymbol{J}_s \boldsymbol{Z}_s^{-1} \boldsymbol{K}_s \boldsymbol{Q} \boldsymbol{J}_m^{-1} \tag{24}$$

$$\boldsymbol{H}_{22} = -(\boldsymbol{J}_s \boldsymbol{Z}_s^{-1} \boldsymbol{K}_s \boldsymbol{J}_s^{-1} + \boldsymbol{I}_{n\times n})^{-1} \boldsymbol{J}_s \boldsymbol{Z}_s^{-1} \boldsymbol{J}_s^T \tag{25}$$

and $\boldsymbol{I}_{n\times n}$ is the n-by-n identity matrix. The 2-port network hybrid matrix will be used later in Section IV to help derive the desired impedance matrices for the impedance controller.

III. Identification of Human Arm Impedance

In this section, we first have an overview of the human arm impedance identification techniques employed in the literature. Then, based on the nature of the therapy tasks and the requirement to not disrupt the normal flow of teleoperation during the interactive phase, we present the human arm impedance strategy that this work utilizes.

A. The Proposed Human Arm Impedance Strategy

The approach seen in [18] used very brief force perturbations to minimize the impact on task execution. Such a scheme will be inconvenient if used in our interactive phase as the motions introduced on the therapist's arm following such disturbances may confuse the patient on the other side of the teleoperation and hamper the execution of the cooperative task. The strategy used in this paper is similar to this approach with the difference that no extra force perturbations are added. Essentially, the very input forces imported by the patient that occur naturally during the telerehabilitation task are regarded as force disturbances, and a relatively short duration of data is used to identify a second-order passive impedance model for the human arm.

A challenge we face is that, unlike [18], we do not have an a priori force perturbation sequence and therefore determining the onset of force perturbations is a challenge. As a workaround, let us first analyze the energy

$$E_{absorbed} = \int_0^T -\boldsymbol{F}_{th}(t)\dot{\boldsymbol{p}}_m(t)\,\mathrm{d}t \tag{26}$$

absorbed by the therapist's arm during a therapy task over timespan T in one Cartesian direction, where the scalar $\boldsymbol{f}_{th}$ denotes the force/torque applied by the therapist's arm on the therapist-side robot in the Cartesian direction under consideration, and the scalar $\boldsymbol{p}_m$ denotes the position of the therapist-side robot's end-effector position measured in that Cartesian direction (therefore also the therapist's arm position since the therapist holds onto the therapist-side robot's end-effector). Although the therapy task may involve movements in multiple Cartesian directions, we will consider only one direction for the time being, and duplicate the process to all of the Cartesian directions involved. As shown in Fig. 3(a) for a typical therapy task in one specific Cartesian direction, each rising edge of the absorbed energy corresponds to a task-relevant force onset in that direction. The energy absorption provides us with a good criterion to determine the onset of force perturbations, as it clearly distinguishes when the arm is moving voluntarily (during initial adjustments of the arm position, for example) from when the arm is moving involuntarily (when the arm is knocked away by the force perturbation). Therefore the onset of a force perturbation in a certain Cartesian direction is determined by the moment when $\dot{E}_{absorbed}$ (which is the time derivative of the absorbed power, $E_{absorbed}$ in (26)) associated with that Cartesian direction becomes positive (i.e. when energy absorption by the arm begins). A typical perturbation onset determination result is shown in Fig. 3(b). As can be seen, it would be difficult to determine the perturbation from the force signal alone as it shows no clear distinction between voluntary movement and involuntary movement.

After the perturbation onset is determined to be at time t_p for each perturbation for one of the Cartesian DOFs involved, we will try to determine the following impedance model for that Cartesian DOF with respect to force and position data in the time window $[t_p,\ t_w]$:

$$\boldsymbol{M}_i\ddot{\boldsymbol{p}}(t) + \boldsymbol{B}_i\dot{\boldsymbol{p}}(t) + \boldsymbol{K}_i\boldsymbol{p}(t) = -\boldsymbol{f}(t),\ \ t \in [t_p,\ t_w] \tag{27}$$

where $\boldsymbol{p}(t) = \boldsymbol{p}_m(t) - \boldsymbol{p}_m(t_p)$, $\boldsymbol{f}(t) = \boldsymbol{F}_{th}(t) - \boldsymbol{F}_{th}(t_p)$ and t_w is a selected time window end. The subscript *i* for the mass-spring-damper model coefficients indicates that the model is identified in the *i*th DOF of the Cartesian space. Note also that we subtract the force and position/velocity/acceleration readings at time t_p in order to consider only the force and position/velocity/acceleration *changes* arising from the disturbance. Classical linear least-squares regression will be used to identify the 1-DOF impedance model in (27).

Determination of t_w in (27) depends on the desired duration of the data window T_w as $t_w = t_p + T_w$. In [18], T_w was chosen to be 200 ms as a compromise between the need to use as little data as possible (to accommodate the 100∼150 ms win-

dow in which the human cannot react voluntarily to the abrupt motion and therefore the arm impedance does not change [20]) and the model identification calculation that requires sufficient data points. In that work, 200 ms was found to provide all-positive impedance values (corresponding to positive $\boldsymbol{M}_i$, $\boldsymbol{B}_i$, $\boldsymbol{K}_i$ in (27)) for over 90% of the perturbations. The need to identify all-positive impedance parameters for the arm in each involved Cartesian DOF is also present in our case because we desire to only obtain the passive impedance of the human arm, as later during the standalone phase, implementing an active impedance may endanger the patient's safety. Furthermore, due to the uncertain nature of the patient-applied (rather than robot-generated) perturbation, we determine a time window length while taking into consideration the goodness of model fit that we measure using the variance accounted for (VAF) test statistic for each perturbation from t_p to $t_p + T_w$, with T_w incrementing from 100 ms to 1000 ms at steps of 10 ms:

$$VAF = 100 \times \left(1 - \frac{var\left(\boldsymbol{F}_{th}(t) - \hat{\boldsymbol{f}}_{th}(t) \right)}{var(\boldsymbol{F}_{th}(t))} \right), \quad t \in [t_p, \ t_w] \tag{28}$$

Here $\hat{\boldsymbol{f}}_{th}(t)$ is the force applied to the therapist-side robot by the therapist's arm as predicted by the identified arm impedance model for a given position trajectory. $\boldsymbol{F}_{th}(t)$ is the actual force applied to the therapist-side robot by the therapist. The upper bound for T_w search is chosen to be 1s as a compromise between the need for a longer window length for impedance model identification and a shorter window for passivity concerns.

Finally, by combining the need to identify all-positive parameters for the impedance model in (27), the need to use data from a short period of time immediately after the perturbation onset, as well as the need for a good model fit, the strategy used to determine T_w associated with the arm impedance model on each involved Cartesian DOF in our work is formulated as follows: for one interactive session, for each involved Cartesian DOF, find the minimum $T_w \in [100 \ ms, 1000 \ ms]$ at 10 ms steps such that the number of all positive-valued identified impedances, Nb_{pos} is maximized subject to the constraint that the average VAF value for the all-positive impedance identification results should be above 95. The algorithm applied to each involved Cartesian DOF is summarized in the flowchart in Fig. 4. The T_w that leads to the maximum Nb_{pos} is then retained and the impedance model parameters identified with this T_w will be used for the next steps.

After determining the 1-DOF model for each Cartesian DOF involved, the complete n-DOF Cartesian arm impedance model can be put together as:

$$\boldsymbol{M}\ddot{\boldsymbol{p}}(t) + \boldsymbol{B}\dot{\boldsymbol{p}}(t) + \boldsymbol{K}\boldsymbol{p}(t) = -\boldsymbol{f}(t), \quad t \in [t_p, \ t_w] \tag{29}$$

where $\boldsymbol{p}(t) = \boldsymbol{p}_{th}(t) - \boldsymbol{p}_{th}(t_p)$ and $\boldsymbol{f}(t) = \boldsymbol{F}_{th}(t) - \boldsymbol{F}_{th}(t_p)$ for the same reasons. The matrices $\boldsymbol{M}$, $\boldsymbol{B}$ and $\boldsymbol{K}$ can be written as

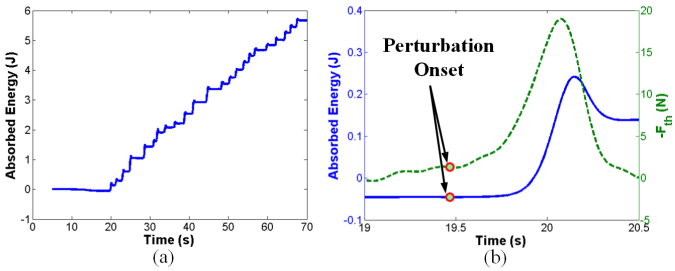

Figure 3: The energy absorbed by the therapist's arm in one Cartesian direction (a) during the entire session of a typical therapy task and (b) within one perturbation (in solid line), superimposed on the force (in dotted line) applied on the therapist's arm by the therapist-side robot. The identified onset of the perturbation is indicated by a red circle on both curves.

$$\boldsymbol{M} = \begin{bmatrix} M_1 & 0 & \cdots & 0 \\ 0 & M_2 & \cdots & 0 \\ \vdots & \vdots & \ddots & \vdots \\ 0 & 0 & \cdots & M_n \end{bmatrix} \tag{30}$$

$$\boldsymbol{B} = \begin{bmatrix} B_1 & 0 & \cdots & 0 \\ 0 & B_2 & \cdots & 0 \\ \vdots & \vdots & \ddots & \vdots \\ 0 & 0 & \cdots & B_n \end{bmatrix} \tag{31}$$

$$\boldsymbol{K} = \begin{bmatrix} K_1 & 0 & \cdots & 0 \\ 0 & K_2 & \cdots & 0 \\ \vdots & \vdots & \ddots & \vdots \\ 0 & 0 & \cdots & K_n \end{bmatrix} \tag{32}$$

A decoupled n-DOF impedance model with $3 \times n$ parameters is used here because otherwise there would have been $3 \times n^2$ parameters to be identified for a complete n-DOF impedance model given less than 1s of data (1000 data points since for our system, the control and data recording operate at 1kHz) via linear least-squares regression, which is very difficult. Therefore, we have decided to simplify the problem by adopting the approach used in [18] in which decoupled models are used. It is important to note that this simplification means the learned impedance is fixed along only the coordinate axes of the reference frame and more complex demonstrations of impedance (where the off-diagonal terms would be non-zero) will not be learned. Additionally, the impedance parameters are treated as time-invariant, although for more complicated upper-limb interactions this may not be the case. In light of these caveats, the proposed approach is appropriate for learning simpler interactions, such as those to be discussed in Section V.

IV. Impedance Control with Disturbance Observer

In this section, we first discuss the impedance controller implemented on the patient-side robot during the standalone phase, once we have the desired impedance parameter $\boldsymbol{M}_d$, $\boldsymbol{B}_d$ and $\boldsymbol{K}_d$. Then we discuss the derivation of the desired impedance to be implemented in the standalone phase.

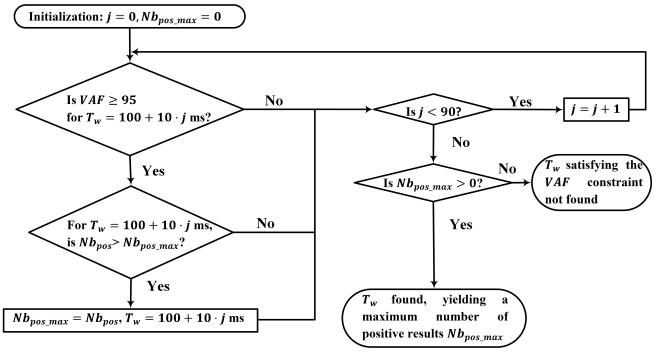

Figure 4: Flowchart showing the algorithm for choosing T_w on the ith Cartesian DOF for an n-DOF ($i \leq n$) task

A. Impedance Controller Design

Impedance control of a robot can be achieved with model-based approaches or model-free approaches. Model-based approaches such as the one introduced in [21] require the exact knowledge of robot dynamics including joint friction. In our application with an industrial robot in the case studies (a 7-DOF SIA5F robot from Yaskawa Motoman, Miamisburg, Ohio, USA, as shown in Fig. 5(b) as the patient-side robot and a 2-DOF planar rehabilitation robot from Quanser, Inc., Markham, Ontario, Canada, as shown in Fig. 5(c) as the therapist-side user interface), while most dynamic terms can be calculated or estimated, the joint friction is hard to obtain. Unlike the therapist-side haptic device which is designed to have low friction, there is considerable friction in the patient-side robot joint that concerns us. The simple yet widely used coulomb + viscous friction model performed poorly because first, the linear model cannot capture the highly nonlinear friction in reality [22]. The model's dependency on velocity also makes static friction compensation ineffective, and in our system, the stiction is very large (in the order of 9 Nm in the joint space). Elaborate nonlinear models such as the ones mentioned in [23] or [24] can capture various nonlinear phenomena such as the Stribeck curve, stiction and pre-sliding displacement, but it is difficult to identify or tune their parameters due to the complexity. In [25] a simpler approach is presented to determine a LuGre model, which is a "dynamic model of friction that describes the behavior of elastic bristles as a function of relative velocity between two surfaces". However, the approach remains largely empirical and requires very refined encoder resolution (especially for measuring the pre-sliding state). Also, the dynamic nature of the LuGre model makes it a potential source of numerical instability in real-time friction compensation implementations.

Given the considerable difficulties associated with determining the robot joint friction precisely, as well as the uncertainties in estimating robot link inertias, we decided to implement an online version of the impedance control based on a nonlinear disturbance observer, which has been used to estimate and compensate for the joint frictions and payload of a robotic device in a trajectory following task [26]. For more details of the nonlinear disturbance observer, readers can refer to [26]. The design of the nonlinear disturbance observer-based impedance control is discussed in the following paragraphs.

Consider the general robot dynamics model for the patient-side robot shown in (9). By assuming that $\hat{\boldsymbol{M}}_s(\boldsymbol{\theta}_s)$ and $\hat{\boldsymbol{N}}_s(\boldsymbol{\theta}_s, \dot{\boldsymbol{\theta}}_s)$ are the estimates of the actual $\boldsymbol{M}_s(\boldsymbol{\theta}_s)$ and $\boldsymbol{N}_s(\boldsymbol{\theta}_s, \dot{\boldsymbol{\theta}}_s)$, and that $\Delta\boldsymbol{M}_s$ and $\Delta\boldsymbol{N}_s$ are the associated uncertainties:

$$\boldsymbol{M}_s(\boldsymbol{\theta}_s) = \hat{\boldsymbol{M}}_s(\boldsymbol{\theta}_s) + \Delta\boldsymbol{M} \tag{33}$$

$$\boldsymbol{N}_s(\boldsymbol{\theta}_s, \dot{\boldsymbol{\theta}}_s) = \hat{\boldsymbol{N}}_s(\boldsymbol{\theta}_s, \dot{\boldsymbol{\theta}}_s) + \Delta\boldsymbol{N} \tag{34}$$

we can define the lumped disturbance vector $\boldsymbol{\tau}_d$ as

$$\boldsymbol{\tau}_d = -\Delta\boldsymbol{M}_s\ddot{\boldsymbol{\theta}}_s - \Delta\boldsymbol{N}_s - \boldsymbol{f}_{rs}(\boldsymbol{\theta}_s, \dot{\boldsymbol{\theta}}_s) \tag{35}$$

in which dynamic uncertainties and joint frictions are lumped into one single disturbance vector. From (9), the patient-side robot dynamics can be re-written into

$$\hat{\boldsymbol{M}}_s(\boldsymbol{\theta}_s)\ddot{\boldsymbol{\theta}}_s + \hat{\boldsymbol{N}}_s(\boldsymbol{\theta}_s, \dot{\boldsymbol{\theta}}_s) = \boldsymbol{\tau}_s + \boldsymbol{\tau}_p + \boldsymbol{\tau}_d \tag{36}$$

For the sake of brevity, the equations describing the nonlinear disturbance observer can be found in the appendix. After getting an estimation of the $\boldsymbol{\tau}_d$ term in (36) with the disturbance observer, we can implement a classic impedance control approach in [21] to achieve the following desired dynamics on the patient-side robot:

$$\boldsymbol{M}_d(\ddot{\boldsymbol{p}}_s - \ddot{\boldsymbol{p}}_{sd}) + \boldsymbol{B}_d(\dot{\boldsymbol{p}}_s - \dot{\boldsymbol{p}}_{sd}) + \boldsymbol{K}_d(\boldsymbol{p}_s - \boldsymbol{p}_{sd}) = \boldsymbol{F}_p \tag{37}$$

where $\boldsymbol{M}_d$, $\boldsymbol{B}_d$, $\boldsymbol{K}_d$ are the desired impedance matrices and $\ddot{\boldsymbol{p}}_{sd}$, $\dot{\boldsymbol{p}}_{sd}$, $\boldsymbol{p}_{sd}$ denote the desired robot acceleration, velocity and position vectors.

Consider the control law

$$\boldsymbol{\tau}_s = \hat{\boldsymbol{M}}_s\boldsymbol{a}_q + \hat{\boldsymbol{N}}_s - \boldsymbol{J}_s^T\boldsymbol{F}_p \tag{38}$$

where $\boldsymbol{a}_q$ is the reference joint acceleration. By combining (6), (36) and (38) we have $\ddot{\boldsymbol{\theta}}_s = \boldsymbol{a}_q$. Let $\boldsymbol{a}_p$ be the reference acceleration in Cartesian space, and let

$$\boldsymbol{a}_p = \boldsymbol{J}_s\boldsymbol{a}_q + \dot{\boldsymbol{J}}_s\dot{\boldsymbol{\theta}}_s \tag{39}$$

or equivalently

$$\boldsymbol{a}_q = \boldsymbol{J}_s^{-1}(\boldsymbol{a}_p - \dot{\boldsymbol{J}}_s\dot{\boldsymbol{\theta}}_s) \tag{40}$$

Together with the kinematic relationship linking joint space acceleration with Cartesian space acceleration:

$$\ddot{\boldsymbol{p}}_s = \boldsymbol{J}_s\ddot{\boldsymbol{\theta}}_s + \dot{\boldsymbol{J}}_s\dot{\boldsymbol{\theta}}_s \tag{41}$$

we have from (37) and (39) that

$$\ddot{\boldsymbol{p}}_s = \boldsymbol{a}_{\boldsymbol{p}} = \ddot{\boldsymbol{p}}_{sd} - \boldsymbol{M}_d^{-1}[\boldsymbol{B}_d(\dot{\boldsymbol{p}}_s - \dot{\boldsymbol{p}}_{sd}) + \boldsymbol{K}_d(\boldsymbol{p}_s - \boldsymbol{p}_{sd}) - \boldsymbol{F}_p] \tag{42}$$

Further, take (42) into (40), and then combining with (38) and the disturbance observer (A.1) we have

$$\boldsymbol{\tau}_s = \hat{\boldsymbol{M}}_s\boldsymbol{J}_s^{-1}\{\ddot{\boldsymbol{p}}_{sd} - \boldsymbol{M}_d^{-1}[\boldsymbol{B}_d(\dot{\boldsymbol{p}}_s - \dot{\boldsymbol{p}}_{sd}) + \boldsymbol{K}_d(\boldsymbol{p}_s - \boldsymbol{p}_{sd}) - \boldsymbol{f}_p] - \dot{\boldsymbol{J}}_s\dot{\boldsymbol{\theta}}_s\} + \hat{\boldsymbol{N}} - \hat{\boldsymbol{\tau}}_d \tag{43}$$

Next, we discuss how the desired impedance is found.

B. Derivation of Desired Impedance

The desired impedance matrices $\boldsymbol{M}_d$, $\boldsymbol{B}_d$ and $\boldsymbol{K}_d$ come from the identified therapist arm impedance $\boldsymbol{Z}_{th}$ as distorted by the teleoperation system dynamics. This is because during the interactive phase, it is the therapist arm impedance after the distortion introduced by the teleoperation system that completes cooperative tasks with the patient. From (21) we can derive that the impedance $\boldsymbol{Z}_d$ displayed to the patient via the patient-side robot during the interactive phase defined by

$$\boldsymbol{F}_p = -\boldsymbol{Z}_d \dot{\boldsymbol{P}}_s \tag{44}$$

is

$$\boldsymbol{Z}_d = \left[\boldsymbol{H}_{21}(\boldsymbol{Z}_{th} - \boldsymbol{H}_{11})^{-1}\boldsymbol{H}_{12} + \boldsymbol{H}_{22}\right]^{-1} \tag{45}$$

where $\boldsymbol{Z}_{th}$ is expressed using the identified $\boldsymbol{M}$, $\boldsymbol{B}$, $\boldsymbol{K}$ matrices identified in Section III as

$$\boldsymbol{Z}_{th} = \boldsymbol{M}s + \boldsymbol{B} + \frac{\boldsymbol{K}}{s} \tag{46}$$

and the $\boldsymbol{H}_{ij}$ are defined from (22) to (25). With respect to Fig. 2, this equates to removing the control and communications channel block and all of the therapist and therapist-side robot components, and replacing them with (43) with inputs from the observer estimate $\hat{\boldsymbol{\tau}}_d$ and the robot joint velocity data $\dot{\boldsymbol{\theta}}_s$.

V. Case Studies

In this section, the proposed LAR telerehabilitation paradigm is applied to two tasks: a 1-DOF task involving a cooperative screwdriver task and a 2-DOF task involving a collaborative peg-in-the-hole task. The 2-DOF task is further supported by including a simulated patient in the trials. We select the screw-driving task since it represents an ADL with synergistic movements similar to opening a doorknob, another common ADL. Peg-in-the-hole tasks have seen use in rehabilitation assessment regimes, such as the Nine-Hole Peg Test [27, 28].

A. 1-DOF Task

1) Therapy Task Description and Robot Configuration: Consider a task in which a screw is driven by the patient into a surface held in position by the therapist as shown in Fig. 5(a). For this screwdriver task to be done in the proposed telerehabilitation context, the patient will be tasked to drive the woodscrew into the wooden plate attached to the end-effector of a patient-side robot (7-DOF SIA5F robot from Yaskawa Motoman, Miamisburg, Ohio, USA, as shown in Fig. 5(b)) that is teleoperated by the therapist from a therapist-side user interface (2-DOF planar rehabilitation robot from Quanser, Inc., Markham, Ontario, Canada, as shown in Fig. 5(c)). Thus, in the interactive phase, while the patient uses a screwdriver to drive the screw into the wooden plate fixed to the patient-side robot, the therapist firmly holds the therapist-side haptic device in position.

Although both the therapist-side and patient-side are multi-DOF robots, they have been configured to accommodate the aforementioned task, which naturally involves only a 1-DOF motion in the Cartesian space. Consider motor 0 of the therapist-side robot and the sixth joint of the patient-side robot corresponding to the joint angles θ_m and θ_s in Fig. 5, respectively. The patient-side position θ_s is made to follow the therapist-side position θ_m while interaction forces at the patient-side side are reflected to the therapist-side side. Because of this 1 to 1 correspondence, Q in Fig.2 becomes $Q = 1$. The second joint of the therapist-side robot is passively (physically) clamped in its home position with the corresponding motor (Motor 1) turned off, while the other 6 joints of the patient-side robot are actively held in position via high-gain PID position control. In Fig. 5, both robots are at their home positions ($\theta_m = \theta_s = 0$). Cartesian frames are attached to the end-effectors of the therapist-side and the patient-side as shown in Fig. 5. Note that for small θ_m and θ_s, the motions of the two robots can be approximated to be along a Cartesian axis. The task is therefore in the Y direction. Through teleoperation, the therapist tries to resist the pushing forces of the patient applied in the Y direction by displaying a stiff impedance to the therapist-side robot in that direction, so that the patient can complete the screwdriver task. The link lengths for the therapist-side and patient-side robot are l_m and l_s respectively, measuring from the rotating axes to the centre of the handle for the therapist-side robot (Fig. 5(c)) and to the screw location on the wooden plate for the patient-side robot (Fig. 5(b)). As a result, the Jacobian matrices in (1) and (2) have become scalars and are

$$J_m = l_m \cos(\theta_m) \tag{47}$$

$$J_s = l_s \cos(\theta_s) \tag{48}$$

respectively. p_m and p_s are therefore measured in the Y direction. 1-DOF interaction forces applied onto the robots by the therapist or the patient: f_{th} and f_p in (5) and (6) are directly measured with two ATI Gamma NET force/torque transducers (Apex, NC, USA) attached to the end-effectors of the two robots at 1 kHz sampling rate. The communication channel is implemented using the Winsock application programming interface over the Ethernet using the UDP protocol at 1 kHz sampling rate – the same rate as the one used in the robot control loops (for reading encoders and issuing torque commands) of both robots. Further, teleoperation system parameters Z_m in (19) can be modeled as an inertia, $Z_m = M_m s$, as we choose to ignore the friction associated with the actuated link of this haptic device. The patient-side robot is modeled as an inertia and a damper because it has significant damping and friction needing to be modeled, leading to $Z_s = M_s s + B_s$ in (20).

2) Experimental Results: During the interactive phase, we use a feedback gain of $K_f = 0.5$ for DFR teleoperation because of the following two reasons: 1) it provides the therapist with a good perception of the perturbations from the patient side; 2) the force feedback is not too strong for the therapist to handle with ease. Numerical values for other teleoperation system parameters are either measured or chosen as shown in Table I. Note that the values for M_m, M_s and B_s are obtained using system identification method similar to what was done in [15]. l_m and l_s are obtained by directly measuring the concerned robot links. K_f, K_v and K_s are directly specified in the controller software.

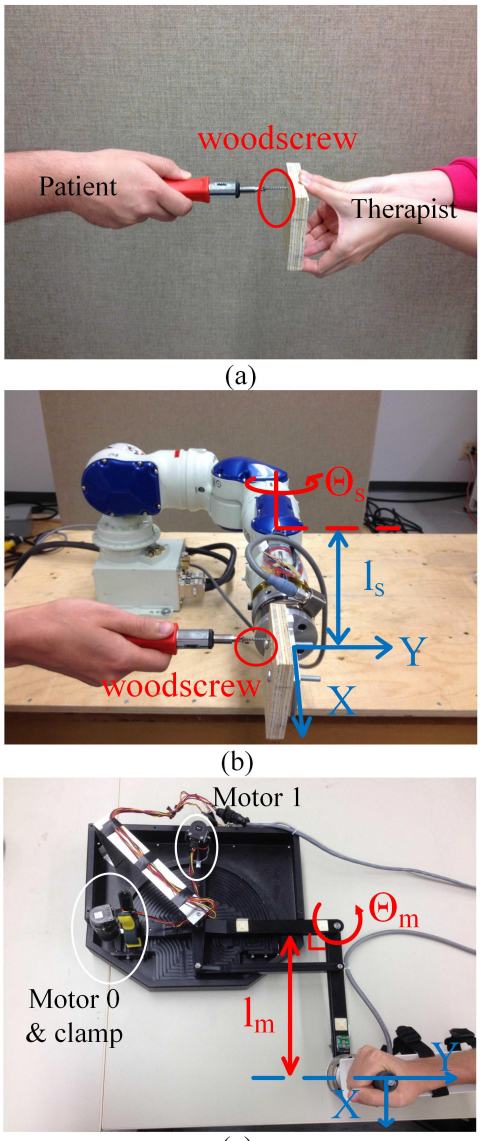

Figure 5: (a) Direction manipulation: the screwdriving task without using any robots. (b) Configuration of the patient-side (patient-side) Yaskawa Motoman SIA5F robot. (c) Configuration of the therapist-side (therapist side-side) rehabilitation robot.

A total of three interactive sessions were carried out, each lasting around 60 s containing 20 to 26 perturbations. The experimental trials were carried out during the same day with one healthy person (the first author of the paper) acting as the therapist and another healthy person (the second author of the paper) acting as the patient. The arm impedance identification results are presented in Table II, including M, B, K, the percentage of all-positive identification results Nb_{pos} over the total number of considered perturbations in each session, and the chosen data window length T_w for model identification.

As can be seen from Table II, with our impedance model identification algorithm shown in Fig. 4, 90% of the perturbations yield all-positive identification results with an average data window length of about 600 ms. We use the averaged impedance parameters: $M = 1.92$ kg, $B = 55.54$ Ns/m and $K = 1454.52$ N/m to to make up the Z_{th} term defined in

Table I: Teleoperation control and analysis parameters

Variable Name	Numerical Value
M_m (kg.m^2)	0.052
M_s (kg.m^2)	0.086
B_s (Nm.s/rad)	7.92
l_m (m)	0.267
l_s (m)	0.267
K_f	0.50
K_v (Nm/rad)	1285.03
K_s (Nm/(rad/s))	36.72

Table II: Therapist arm impedance identification results

Session	M (kg)	B (Ns/m)	K (N/m)	$\frac{Nb_{pos}}{Nb_{tot}}$	T_w (ms)
1	1.48	60.87	1085.80	75%	420
2	1.70	52.48	1733.83	100%	530
3	2.61	53.23	1543.95	96%	860
Average	1.92	55.54	1454.52	90%	603
SD	0.60	4.64	333.14	13%	229

(46). Combining with the definition in (45), the displayed impedance during interactive phase Z_d can be numerically approximated into the following form for impedance control implementation

$$Z_d \approx M_d s + B_d + \frac{K_d}{s} \tag{49}$$

with $M_d = 3.89$ kg, $B_d = 160.14$ Ns/m and $K_d = 3467.36$ N/m following an optimization operation.

In the standalone phase, the patient-side robot is programmed under the impedance control law specified in (43) with the parameters of M_d, B_d and K_d found in interactive phase discussed in the previous subsection. For this 1-DOF screwdriving task under consideration, $\ddot{p}_{sd}$, $\dot{p}_{sd}$ and p_{sd} in (43) are all 0. For the disturbance observer, we need to first find Y using (A.8) from the parameters ζ, β and σ_2. Since the dynamics are in 1-DOF, M_s does not vary over time. Therefore ζ, representing an upper bound of $\dot{\hat{M}}_s$, is zero. σ_2, being an upper bound of $\hat{M}_s$, can be taken as the same value of $\hat{M}_s$. While the value of M_s, or the theoretical value of the patient-side robot inertia provides a good candidate for $\hat{M}_s$ (therefore σ_2, in practice it is tuned together with β for best observer convergence while being able to reject noise and instability). Through experiments, we take $\hat{M}_s = \sigma_2 = 0.15$ and $\beta = 1050$ for the disturbance observer.

The patient (imitated by a healthy person) is then able to complete the screwdriver task with the patient-side robot alone in this phase. The impedance control implementation is validated by comparing the actual patient-side robot position against the simulated patient-side robot position based on the desired impedance and the measured interaction forces. Based on the therapists arm impedance that was retrieved during the interactive phase, patient-side robot positions upon perturbation are simulated. This simulation is the ideal movement, based on the therapists arm impedance, that we hope the patient-side robot will do in response to measured interaction forces. However, factors such as the patient-side robots inertia

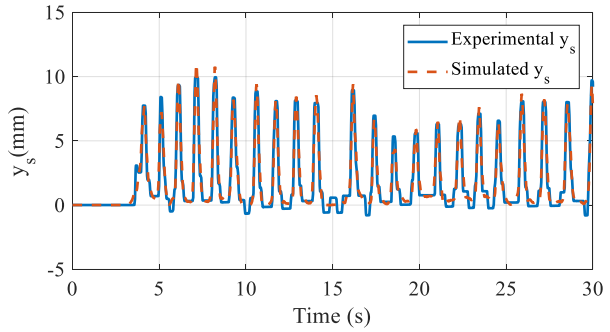

Figure 6: Comparison between simulated position based on force measurement and the actual position during standalone phase (Error$_{RMS}$ = 0.6550 mm).

and joint friction may impact the actual performance of the robot in replicating these movements. The graph shows the comparison between the simulated (ideal) movement of the patient-side robot vs its actual movement.

The comparison result is plotted in Fig. 6 where a good match is shown. Note that the effect of the strong stiction inherent in our industrial manipulator arm is still visible but it is mitigated (position error no more than 1 mm during the task) thanks to the disturbance observer approach. We can also see from Fig. 6 that the maximum displacement in the Y direction of the patient-side arm is around 12 mm, which is also the case in the interactive phase, showing that the desired behaviour has been successfully mapped from the therapist to the patient-side robot during the standalone phase.

B. 2-DOF Task

1) Therapy Task Description and Robot Configuration: The 2-DOF task consists of the patient trying to put an aluminum mechanical part representing a 1-dimensional "hole" onto a peg held by the therapist as shown in Fig. 7(a). In the proposed LAR paradigm, the patient will insert the hole onto the peg attached to the end-effector of the patient-side robot shown in Fig. 7(b), which is teleoperated by the therapist from the therapist-side interface shown in Fig. 7(c). While "hole-onto-the-peg" insertion seems to be a more appropriate term to name the considered task, since the peg and the hole play interchangeable roles, we still name the task "peg-in-the-hole" insertion. The peg-in-the-hole insertion task is a challenging manipulation task, involving both position and force control. In our case, the task requires the patient to first align the hole with the peg by wiggling it primarily in the Y direction, illustrated in Fig. 8(a). This procedure is made possible by the curved opening of the hole as well as the curvature of the peg tip. This step is also shown in Fig. 7(a) in the direction manipulation case, where no robots are involved. Once the hole and the peg are lined up (illustrated in Fig. 8(b)), the patient pushes the hole onto the peg by exerting a force in the X direction (illustrated in Fig. 8). The X and Y Cartesian directions are defined for the patient-side robot in Fig. 7(b). Note that the X-Y frame origin is placed at the centre of the peg tool when the patient-side robot is at home position, and it does not move with the peg tool. We name this frame the patient-side base frame. For the therapist-side robot, X and Y Cartesian directions are the same as the patient-side robot and the frame origin is attached to the handle when the therapist-side robot is at its home position. Although the therapist-side frame origin is also defined using the end-effector, it doesn't move with the handle either once it is defined. We name this X-Y frame related to the therapist-side robot, the therapist-side base frame. Note that the therapist-side robot is not at its home position in Fig. 7(c). The therapist-side robot is at its home position when θ_{1m} and θ_{2m} shown in Fig. 7(c) are both zero. Axes parallel to the X and Y-axis of the therapist-side robot but attached to the robot centre axis shown as X_0 and Y_0 in Fig. 7(c), which will be used later for details on the joint angle definition for the therapist-side robot.

Similar to the 1-DOF task screwdriver task, the therapist holds firmly the therapist-side haptic device in both X and Y directions while the patient tries to complete the task during the interactive phase. We make this choice because it is desirable for the patient to learn to behave compliantly. For the peg-in-the-hole task to be able to be completed, both operators cannot be both compliant or both rigid at the same time (or else the hole risks not being able to be lined up with and inserted into the peg).

In this task, we face the difficulty of teleoperating two robots with different kinematics, workspaces and DOFs, because of our choice of the therapist-side and patient-side robots. We solve this problem by making the robot with more DOFs and a larger workspace have a similar effective geometry as the robot with fewer DOFs and a smaller workspace. To do so, we make the 7-DOF patient-side robot take on an effective 2-DOF geometry. The 1st, 4th and 6th joints of the patient-side robot are arranged according to inverse kinematics such that the distance between the 1st joint axis and the 6th joint axis, which is l_{1s} in Fig. 7(b), takes on a desired value and becomes the length of the 1st "effective link" of the patient-side robot.

During teleoperation, high gain PID control is applied to joints 2 to 5 of the patient-side robot to maintain this geometry. The 2nd "effective link" of the patient-side robot is the same as the actuated link presented in the 1-DOF case study (comprising the last link of the patient-side robot, the force sensor and peg tool) with link length l_{2s} as shown in Fig. 7(b). For the therapist-side robot, both robot joints are actuated and the link lengths are l_{1m} and l_{2m} respectively, as shown in Fig. 7(c). Note that l_{2m} is the same as l_m for the 1-DOF screwdriver task. We define that at home position, the 1st effective link and the 2nd effective link of the patient-side robot are perpendicular to each other (shown in Fig. 7(b)), while the 2nd effective link points to the positive X direction. The same can be said about the therapist-side robot: at home position, the 1st link and the 2nd link are perpendicular to one another, while the 2nd link points to the positive X direction.

In terms of joint angles, we use the 1st and 6th joint angle of the patient-side robot minus their values when the patient-side robot is at its home position as the new joint angles: θ_{1s} and θ_{2s}. Therefore, at the home position shown in Fig. 7(b), $\theta_{1s} = \theta_{2s} = 0$. For the therapist-side robot, we define the 1st joint angle to be the angle formed by rotating the Y_0 axis counterclockwise around the robot centre joint to be parallel to the 1st robot link (l_{1m}), and the 2nd joint angle to be the angle

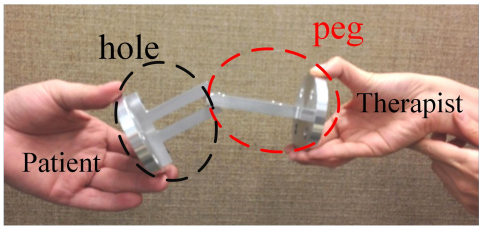

(a)

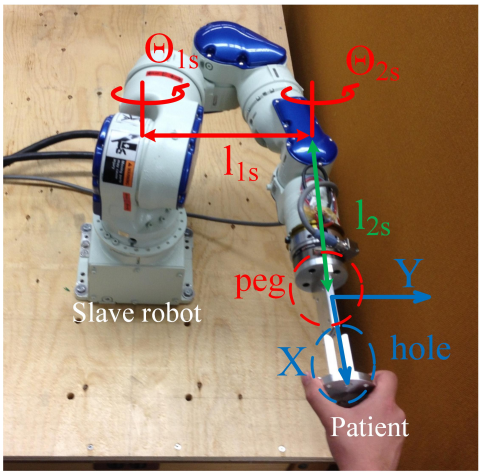

(b)

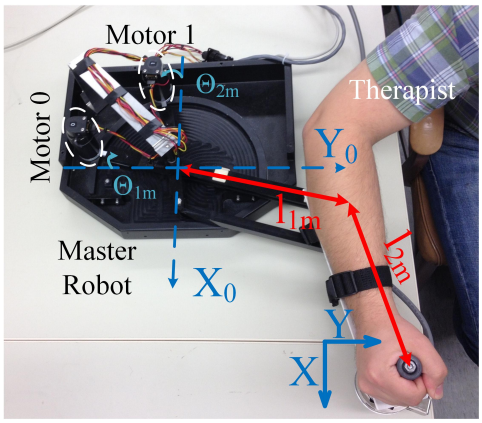

(c)

Figure 7: (a) Direct manipulation: The peg-in-the-hole task without using any robots. (b) Configuration of the patient-side (patient-side) Yaskawa Motoman SIA5F robot as the patient-side. (c) Configuration of the therapist-side (therapist-side) rehabilitation robot as the therapist-side.

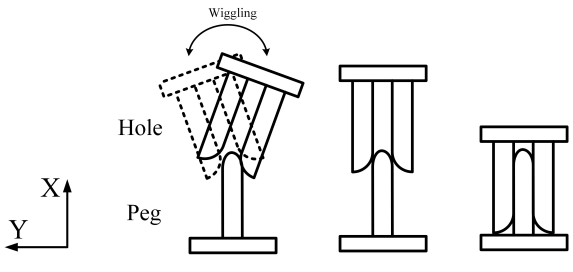

(a) (b) (c)

Figure 8: Illustration of the peg-in-the-hole task. (a) Wiggling of the hole in the Y direction. (b) Alignment of the peg and the hole. (c) The hole pushed onto the peg.

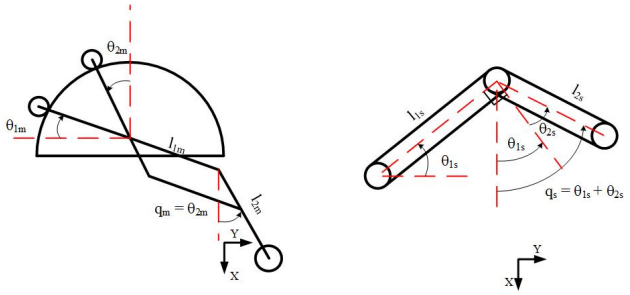

(a) (b)

Figure 9: Illustration of (a) the therapist-side robot and (b) the patient-side robot joint angle configurations.

formed by rotating the X_0 axis counterclockwise to be parallel to the 2nd robot link (l_{2m}). Note that in the configuration presented in Fig. 7(c), θ_{1m} has a negative value while θ_{2m} has a positive value. The joint angle configurations for the therapist-side and the patient-side are illustrated in Fig. 9.

We made $l_{1s} = l_{1m} = 0.254$ m. As we saw in the 1-DOF task, $l_{2s} = l_{2m} = 0.2667$ m (listed in Table I). Therefore, we have made the therapist-side and patient-side robots have similar effective geometries. During teleoperation, we simply make the patient-side robot follow the therapist-side robot by using the current values of θ_{1m} and $\theta_{2m} - \theta_{1m}$ as the reference positions for θ_{1s} and θ_{2s}. This feature can be seen from from Fig. 9, by defining the angles between the X-axis and the second link of both robots (l_{2m} and l_{2s}) as q_m and q_s respectively. Since q_m and q_s should be equal to each other, we have

$$q_m = \theta_{2m} = q_s = \theta_{1s} + \theta_{2s} \tag{50}$$

Therefore,

$$\theta_{2m} = \theta_{1s} + \theta_{2s} \tag{51}$$

$$\theta_{2s} = \theta_{2m} - \theta_{1s} \tag{52}$$

Since θ_{1s} takes θ_{1m} as its reference, we can replace θ_{1s} in (52) by θ_{1m} and obtain

$$\theta_{2s} = \theta_{2m} - \theta_{1m} \tag{53}$$

as the reference angle position for θ_{2s}. This feature makes $\boldsymbol{Q}$ in Fig. I take the following form:

$$\boldsymbol{Q} = \begin{bmatrix} 1 & 0 \\ -1 & 1 \end{bmatrix} \tag{54}$$

To recapitulate mathematically the above description of the robot geometries, if we express Cartesian positions $\boldsymbol{p}_m$ and $\boldsymbol{p}_s$ as $[x_m\ y_m]^T$ and $[x_s\ y_s]$ respectively, where x and y represent the Cartesian coordinate on the X and Y axis, then $\boldsymbol{p}_m$ and

$\boldsymbol{p}_s$ can be expressed as

$$\begin{aligned}\boldsymbol{p}_m &= \begin{bmatrix} x_m \\ y_m \end{bmatrix} \\ &= \begin{bmatrix} -l_{1m}\sin(\theta_{1m}) + l_{2m}\cos(\theta_{2m}) - l_{2m} \\ l_{1m}\cos(\theta_{1m}) + l_{2m}\sin(\theta_{2m}) - l_{1m} \end{bmatrix} \end{aligned} \tag{55}$$

$$\begin{aligned}\boldsymbol{p}_s &= \begin{bmatrix} x_s \\ y_s \end{bmatrix} \\ &= \begin{bmatrix} -l_{1s}\sin(\theta_{1s}) + l_{2s}\cos(\theta_{1s}+\theta_{2s}) - l_{2s} \\ l_{1s}\cos(\theta_{1s}) + l_{2s}\sin(\theta_{1s}+\theta_{2s}) - l_{1s} \end{bmatrix} \end{aligned} \tag{56}$$

Accordingly, Jacobian matrices $\boldsymbol{J}_m$ and $\boldsymbol{J}_s$ in (1) and (2) become

$$\boldsymbol{J}_m = \begin{bmatrix} -l_{1m}\cos(\theta_{1m}) & -l_{2m}\sin(\theta_{2m}) \\ -l_{1m}\sin(\theta_{1m}) & l_{2m}\cos(\theta_{2m}) \end{bmatrix} \tag{57}$$

$$\boldsymbol{J}_s = \begin{bmatrix} -l_{1s}\cos(\theta_{1s}) - l_{2s}\sin(\theta_{1s}+\theta_{2s}) & -l_{2s}\sin(\theta_{1s}+\theta_{2s}) \\ -l_{1s}\sin(\theta_{1s}) + l_{2s}\cos(\theta_{1s}+\theta_{2s}) & l_{2s}\cos(\theta_{1s}+\theta_{2s}) \end{bmatrix} \tag{58}$$

2) Experimental Results: During the interactive phase, a series of 11 peg-in-the-hole insertion tasks was completed via teleoperation. The experimental trials were carried out during the same day with one healthy person (first author of the paper) acting as the therapist and another healthy person (second author of the paper) acting as the patient. The force feedback gains for the therapist-side robot in (12) and the position control gains for the patient-side robot in (11) were chosen to be

- $K_{f1} = 0.3$, $K_{f2} = 0.3$
- $K_{p1} = 4629.50$ Nm/rad, $K_{v1} = 57.87$ Nm/(rad/s), $K_{p2} = 1468.61$ Nm/rad, $K_{v2} = 18.36$ Nm/(rad.s)

While the tasks were being completed, the position and force data on the therapist's side were recorded. The T_w search algorithm presented in Fig. 4 yields 960 ms for the X direction and 170 ms for the Y direction. By using the technique described in Section III, we obtain the following identification results for the therapist's arm impedance in (30):

- $M_1 = 3.379$ kg, $B_1 = 25.15$ Ns/m, $K_1 = 980.552$ N/m
- $M_2 = 0.518$ kg, $B_2 = 12.96$ Ns/m, $K_2 = 112.617$ N/m

where the subscripts 1 and 2 represent the X and Y directions respectively

We can see that the arm demonstrates a stiffer impedance along the X direction, which agrees with the findings of [15]. We can write $\boldsymbol{Z}_{th}$ as

$$\boldsymbol{Z}_{th} = \begin{bmatrix} 3.379s + 25.15 + \dfrac{980.552}{s} & 0 \\ 0 & 0.518s + 12.96 + \dfrac{112.617}{s} \end{bmatrix} \tag{59}$$

Now we need to find the the impedance displayed to the patient during the interactive phase $\boldsymbol{Z}_d$ in (45). By applying a persistent perturbation to the therapist-side robot, we can identify the following linearized form of (19)

$$\boldsymbol{Z}_m \approx \begin{bmatrix} 0.0556 & 0.0077 \\ 0.0077 & 0.0687 \end{bmatrix} s + \begin{bmatrix} 0.0942 & 0 \\ 0 & 0.0731 \end{bmatrix} \tag{60}$$

by taking into account the fact that the therapist-side robot's end-effector moves around its zero position. Similarly we can obtain the linearized form of (20):

$$\boldsymbol{Z}_s \approx \begin{bmatrix} 1.35 & 0.086 \\ 0.086 & 0.086 \end{bmatrix} s + \begin{bmatrix} 15.3 & 0 \\ 0 & 9.5 \end{bmatrix} \tag{61}$$

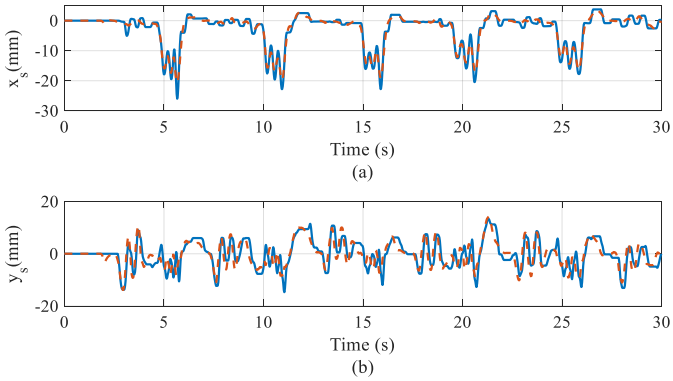

Figure 10: Comparison between simulated positions based on force measurement (dashed red lines) and the actual positions (solid blue lines) during standalone phase. (a) X direction ($\text{Error}_{RMS} = 1.1946$ mm), (b) Y direction ($\text{Error}_{RMS} = 3.2927$ mm).

By taking the numerical values of $\boldsymbol{J}_m$, $\boldsymbol{J}_s$, $\boldsymbol{K}_f$, $\boldsymbol{K}_s$, $\boldsymbol{Z}_m$ and $\boldsymbol{Z}_s$ into (22)-(25) and (45), we can get the following parameters ready for impedance control implementation following an optimization approach:

$$\boldsymbol{M}_d = \begin{bmatrix} 9.77 & 0 \\ 0 & 1.23 \end{bmatrix} \text{ Kg} \tag{62}$$

$$\boldsymbol{B}_d = \begin{bmatrix} 180.56 & 0 \\ 0 & 60.82 \end{bmatrix} \text{ Ns/m} \tag{63}$$

$$\boldsymbol{K}_d = \begin{bmatrix} 2316.20 & 0 \\ 0 & 360.233 \end{bmatrix} \text{ N/m} \tag{64}$$

In the standalone phase, the patient-side robot is programmed to demonstrate the desired impedance (37) via the controller (43). With trial-and-error, the best disturbance observer was obtained with the following parameters for (A.8):

$$\begin{aligned} \zeta &= 10 \text{ Nm.s/rad} \\ \beta &= 50 \text{ Nm.s/rad} \\ \sigma_2 &= 10 \end{aligned}$$

The patient (imitated by a healthy person) is then able to complete the peg-in-the-hole task with the patient-side robot alone in this phase. We repeated the peg-in-the-hole insertion task in the absence of the therapist for several of times. The task was completed successfully with the patient-side robot alone. If the robot impedance was not controlled properly, the robot could yield to pressure from the patient and the task would fail. The impedance control implementation is validated by comparing the actual robot position in both X and Y directions with what the target impedance model predicts based on the measured forces. A good match in both directions is shown in Fig. 10. The desired behaviour has therefore been successfully mapped from the therapist to the patient-side robot during the standalone phase for the 2-DOF peg-in-the-hole insertion task.

C. 2-DOF Task with Simulated Patient

Following the same procedure as the previous peg-in-the-hole trial and using the same gains, two healthy persons (different people compared from the previous trial) took the role of the therapist and the patient. However, this time we simulated a patient with arm tremors using a Transcutaneous Electrical Nerve Stimulation (TENS) device. Two electrodes were attached to the acting patient's forearm and were set to provide stimulation at roughly 3 Hz. The stimulation of the upper arm and wrist at low frequency induces a behavior similar to post-stroke patients [29].

The T_w search algorithm yields 170 ms for the X direction and 240 ms for the Y direction. The therapist's arm impedance is:

- M_1 = 1.883 kg, B_1 = 22.235 Ns/m, K_1 = 294.599 N/m
- M_2 = 0.182 kg, B_2 = 5.847 Ns/m, K_2 = 194.156 N/m

It can be seen that the arm is stiffer in the X direction but is less stiff when compared to the therapist impedance from the previous trial. This feature can be attributed to a different person acting as the therapist.

Since the Z_m and Z_s parameters come from robot identification, they remain unchanged. After the optimization approach, the following desired impedance parameters are determined:

$$\boldsymbol{M}_d = \begin{bmatrix} 4.941 & 0 \\ 0 & 1.871 \end{bmatrix} \text{ Kg} \tag{65}$$

$$\boldsymbol{B}_d = \begin{bmatrix} 80.524 & 0 \\ 0 & 82.760 \end{bmatrix} \text{ Ns/m} \tag{66}$$

$$\boldsymbol{K}_d = \begin{bmatrix} 911.294 & 0 \\ 0 & 591.73 \end{bmatrix} \text{ N/m} \tag{67}$$

In the standalone phase, the disturbance observer parameters are found using trial-and-error:

$$\zeta = 3 \text{ Nm.s/rad} \tag{68}$$

$$\beta = 50 \text{ Nm.s/rad} \tag{69}$$

$$\sigma_2 = 0.5 \tag{70}$$

As seen in Fig. 11, the Motoman Robot, put under impedance control, can match the movement of a simulated patient with tremors in the standalone phase. The TENS device produced wrist flexion and extension, resulting in more movement in the Y direction.

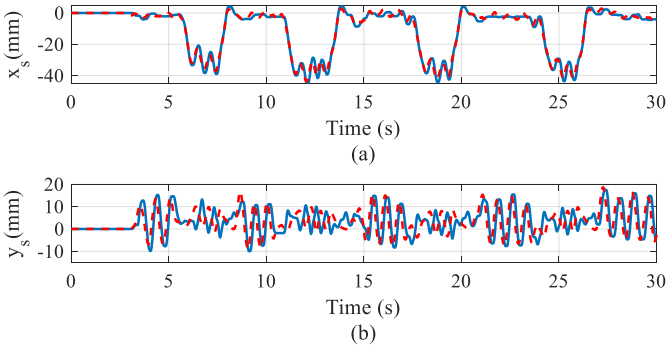

Figure 11: Simulated Patient Trial. Comparison between simulated positions based on force measurement (dashed red line) and the actual positions (solid blue line) during standalone phase. (a) X direction (Error_{RMS} = 1.7196 mm), (b) Y direction (Error_{RMS} = 4.9557 mm). The tremors due to the TENS device are more prominent in the Y direction.

VI. Conclusions and Future Work

In this study, we proposed and demonstrated a novel telerehabilitation approach: The learn-and-replay (LAR) over two collaborative tasks: a screwdriver task and a peg-in-the-hole insertion task. During the interactive phase, the therapist supported the patient in completing the task and simultaneously the impedance of his arm was measured by the therapist-side haptic device. It is worth noting that the interactive phase should last long enough in time to allow a sufficient number of task repetitions to take place for impedance model identification. In the case studies of this paper, we found that a few minutes' of interaction provided enough data for impedance identification. The measured impedance was then processed taking into account the teleoperation system dynamics to obtain the desired impedance parameters used for impedance control implementation during the standalone phase. In the standalone phase, the impedance control was successfully implemented on the patient-side robot and the therapist's role in completing the tasks was successfully replicated by the patient-side robot. We showed the feasibility of the proposed LAR telerehabilitation paradigm and its potential in time-sharing a therapist and thus partly automating the rehabilitation therapy.

One important caveat regarding the formulation of the learned impedance behavior used in this work is that the impedance is regarded as time-invariant and fixed along the coordinate axes. We acknowledge this as a potential limitation to our approach, given the knowledge that therapeutic assistance is often provided in a time-varying and direction-dependent manner with respect to the task. Another consideration is to explore different methods of selecting the desired impedance matrices, instead of only considering the mean of the fitted values which is prone to outliers. This could include taking the median of the values, or fitting the parameters in a coordinate space that better encompasses the behavior of the responses such as the natural frequency of the impedance.

In the future, new multi-DOF tasks that are closely related to current rehabilitation practices for upper-limb rehabilitation can be designed. The tasks need to be closely related to activities of daily living (ADL) and therapist evaluation of the paradigm will be focused on. Doing so will likely require reformulating the method of learning impedance to consider tasks as dynamic and trajectory-based. Clinical patient-oriented studies will be carried out to study the usefulness of the proposed paradigm in real clinical settings.

Appendix

Nonlinear Disturbance Observer

The following is the nonlinear disturbance observer used to estimate $\boldsymbol{\tau}_d$. Similar to [26], the nonlinear disturbance observer

can be written as:

$$\begin{aligned}
\dot{\boldsymbol{z}} &= -\boldsymbol{L}(\boldsymbol{\theta}_s, \dot{\boldsymbol{\theta}}_s)\boldsymbol{z} + \boldsymbol{L}(\boldsymbol{\theta}_s, \dot{\boldsymbol{\theta}}_s)\{\hat{\boldsymbol{N}}_s - \boldsymbol{\tau_s} - \boldsymbol{\tau_p} - \boldsymbol{p}(\boldsymbol{\theta}_s, \dot{\boldsymbol{\theta}}_s)\} \\
\hat{\boldsymbol{\tau}}_d &= \boldsymbol{z} + \boldsymbol{p}(\boldsymbol{\theta}_s, \dot{\boldsymbol{\theta}}_s) \\
\frac{d}{dt}\boldsymbol{p}(\boldsymbol{\theta}_s, \dot{\boldsymbol{\theta}}_s) &= \boldsymbol{L}(\boldsymbol{\theta}_s, \dot{\boldsymbol{\theta}}_s)\hat{\boldsymbol{M}}_s(\boldsymbol{\theta}_s)\ddot{\boldsymbol{\theta}}_s
\end{aligned} \tag{A.1}$$

where $\hat{\boldsymbol{\tau}}_d$ denotes the estimated disturbance vector, and the vectors $\boldsymbol{p}(\boldsymbol{\theta}_s, \dot{\boldsymbol{\theta}}_s)$ and $\boldsymbol{z}$ are introduced as auxiliary variables to construct the observer, and $\boldsymbol{L}(\boldsymbol{\theta}_s, \dot{\boldsymbol{\theta}}_s)$ is the observer gain matrix. Note that although unlike [26] where patient (patient-side) robot interactions $\boldsymbol{\tau}_s$ would be grouped into the disturbance term $\boldsymbol{\tau}_d$ because we measure it directly with a force sensor, the observer design method derived in [26] is still valid and we still have the same disturbance estimation error dynamics:

$$\Delta\dot{\boldsymbol{\tau}}_d = \dot{\boldsymbol{\tau}}_d - \boldsymbol{L}(\boldsymbol{\theta}_s, \dot{\boldsymbol{\theta}}_s)\Delta\boldsymbol{\tau}_d \tag{A.2}$$

where $\Delta\boldsymbol{\tau}_d = \boldsymbol{\tau}_d - \hat{\boldsymbol{\tau}}_d$.

To complete the nonlinear observer design, we can use the following two steps [26] to determine $\boldsymbol{L}(\boldsymbol{\theta}_s, \dot{\boldsymbol{\theta}}_s)$ and $\boldsymbol{p}(\boldsymbol{\theta}_s, \dot{\boldsymbol{\theta}}_s)$:

1) Find invertible matrix $\boldsymbol{Y}$, solution to the following linear matrix inequality (LMI):

$$\begin{bmatrix} \boldsymbol{Y} + \boldsymbol{Y}^T - \zeta\boldsymbol{I} & \boldsymbol{Y}^T \\ \boldsymbol{Y} & \boldsymbol{\Gamma}^{-1} \end{bmatrix} \geq 0 \tag{A.3}$$

   where $\boldsymbol{I}$ is the identity matrix of the corresponding order, $\boldsymbol{\Gamma}$ is a positive definite and symmetric matrix and ζ is an upper bound of $\|\dot{\hat{\boldsymbol{M}}}_s(\boldsymbol{\theta}_s)\|$[1]
2) Define the disturbance observer gain matrix as

$$\boldsymbol{L}(\boldsymbol{\theta}_s) = \boldsymbol{Y}\hat{\boldsymbol{M}}_s^{-1}(\boldsymbol{\theta}_s) \tag{A.4}$$

   and as a result of (A.1) and (A.4) we have

$$\boldsymbol{p}(\boldsymbol{\theta}_s) = \boldsymbol{Y}\dot{\boldsymbol{\theta}}_s \tag{A.5}$$

The above process guarantees that in the presence of fast-varying disturbances, which is our case because of friction, the disturbance tracking error $\Delta\boldsymbol{\tau}_d$ is globally uniformly ultimately bounded [26], and that the tracking error converges with an exponential rate of $(1-\alpha)\lambda_{min}(\boldsymbol{\Gamma})/2\sigma_2\|\boldsymbol{Y}^{-1}\|^2$ to a ball with radius $2\kappa\sigma_2\|\boldsymbol{Y}^{-1}\|^2/\alpha\lambda_{min}(\boldsymbol{\Gamma})$. α is a scalar satisfying $0 < \alpha < 1$, $\lambda_{min}(.)$ denotes the minimum eigenvalue of a square matrix, scalar κ defines the bound for the rate of change of the lumped disturbance:

$$\|\dot{\boldsymbol{\tau}}_d(t)\| \leq \kappa, \forall t > 0 \tag{A.6}$$

and the scalar σ_2 is defined with the following inequality for all $\boldsymbol{\theta}_s$ in the work space:

$$\sigma_1\boldsymbol{I} \leq \hat{\boldsymbol{M}}(\boldsymbol{\theta}_s) \leq \sigma_2\boldsymbol{I} \tag{A.7}$$

Further, If we choose $\boldsymbol{Y}$ to be of the form $y\boldsymbol{I}$ and assume that $\boldsymbol{\Gamma}$ takes the form $\boldsymbol{\Gamma} = \gamma\boldsymbol{I}$ with y and γ being scalars, an optimal analytical solution exists for (A.3) [26]:

$$\boldsymbol{Y}_{optimal} = \frac{1}{2}(\zeta + 2\beta\sigma_2)\boldsymbol{I} \tag{A.8}$$

where β is the minimum tracking error convergence rate to be chosen. This solution takes into account the need to reduce sensitivity to noise during disturbance rejection.

[1]In this paper, the vector norm (vector 2-norm) and matrix norm (induced matrix 2-norm) are defined as (unless otherwise stated): $\|\boldsymbol{x}\| = \sqrt{\boldsymbol{x}^T\boldsymbol{x}}, \forall \boldsymbol{x} \in R^n$; $\|\boldsymbol{X}\| = \sqrt{\lambda_{max}(\boldsymbol{X}^T\boldsymbol{X})}, \forall \boldsymbol{X} \in R^{n\times n}$ where $\lambda_{max}(.)$ denotes the maximum eigenvalue of a square matrix

REFERENCES

[1] H. I. Krebs, J. J. Palazzolo, L. Dipietro, M. Ferraro, J. Krol, K. Rannekleiv, B. T. Volpe, and N. Hogan, "Rehabilitation robotics: Performance-based progressive robot-assisted therapy," *Autonomous robots*, vol. 15, no. 1, pp. 7–20, 2003.

[2] D. W. Franklin, R. Osu, E. Burdet, M. Kawato, and T. E. Milner, "Adaptation to stable and unstable dynamics achieved by combined impedance control and inverse dynamics model," *Journal of neurophysiology*, vol. 90, no. 5, pp. 3270–3282, 2003.

[3] R. Osu, E. Burdet, D. W. Franklin, T. E. Milner, and M. Kawato, "Different mechanisms involved in adaptation to stable and unstable dynamics," *Journal of Neurophysiology*, vol. 90, no. 5, pp. 3255–3269, 2003.

[4] E. Burdet, R. Osu, D. W. Franklin, T. E. Milner, and M. Kawato, "The central nervous system stabilizes unstable dynamics by learning optimal impedance," *Nature*, vol. 414, no. 6862, pp. 446–449, 2001.

[5] G. Ganesh, A. Albu-Schäffer, M. Haruno, M. Kawato, and E. Burdet, "Biomimetic motor behavior for simultaneous adaptation of force, impedance and trajectory in interaction tasks," in *2010 IEEE International Conference on Robotics and Automation*. IEEE, 2010, pp. 2705–2711.

[6] K. Kronander and A. Billard, "Online learning of varying stiffness through physical human-robot interaction," in *2012 IEEE International Conference on Robotics and Automation*. Ieee, 2012, pp. 1842–1849.

[7] L. Rozo, S. Calinon, D. Caldwell, P. Jiménez, and C. Torras, "Learning collaborative impedance-based robot behaviors," in *AAAI Conference on Artificial Intelligence*, 2013, pp. 1422–1428.

[8] C. R. Carignan and H. I. Krebs, "Telerehabilitation robotics: bright lights, big future?" *Journal of rehabilitation research and development*, vol. 43, no. 5, p. 695, 2006.

[9] S. F. Atashzar, M. Shahbazi, M. Tavakoli, and R. V. Patel, "A new passivity-based control technique for safe patient-robot interaction in haptics-enabled rehabilitation systems," in *2015 IEEE/RSJ International Conference on Intelligent Robots and Systems (IROS)*, Sept 2015, pp. 4556–4561.

[10] M. Shahbazi, S. F. Atashzar, M. Tavakoli, and R. V. Patel, "Therapist-in-the-loop robotics-assisted mirror rehabilitation therapy: An assist-as-needed framework," in *2015 IEEE International Conference on Robotics and Automation (ICRA)*, 2015, pp. 5910–5915.

[11] F. A. Mussa-Ivaldi, N. Hogan, and E. Bizzi, "Neural, mechanical, and geometric factors subserving arm posture

in humans," *The Journal of Neuroscience*, vol. 5, no. 10, pp. 2732–2743, 1985.

[12] H. Gomi, Y. Koike, and M. Kawato, "Human hand stiffness during discrete point-to-point multi-joint movement," in *1992 14th Annual International Conference of the IEEE Engineering in Medicine and Biology Society*, vol. 4, Oct 1992, pp. 1628–1629.

[13] J. M. Dolan, M. B. Friedman, and M. L. Nagurka, "Dynamic and loaded impedance components in the maintenance of human arm posture," *IEEE Transactions on Systems, Man and Cybernetics*, vol. 23, no. 3, pp. 698–709, 1993.

[14] H. Gomi and M. Kawato, "Equilibrium-point control hypothesis examined by measured arm stiffness during multijoint movement," *Science*, vol. 272, no. 5258, pp. 117–120, 1996.

[15] M. Dyck, "Measuring the dynamic impedance of the human arm," Master's thesis, University of Alberta, 2013.

[16] T. Tsuji, P. G. Morasso, K. Goto, and K. Ito, "Human hand impedance characteristics during maintained posture," *Biological cybernetics*, vol. 72, no. 6, pp. 475–485, 1995.

[17] E. Burdet, R. Osu, D. Franklin, T. Yoshioka, T. Milner, and M. Kawato, "A method for measuring endpoint stiffness during multi-joint arm movements," *Journal of biomechanics*, vol. 33, no. 12, pp. 1705–1709, 2000.

[18] M. S. Erden and A. Billard, "End-point impedance measurements at human hand during interactive manual welding with robot," in *2014 IEEE International Conference on Robotics and Automation (ICRA)*, May 2014, pp. 126–133.

[19] M. Tavakoli, A. Aziminejad, R. Patel, and M. Moallem, "High-fidelity bilateral teleoperation systems and the effect of multimodal haptics," *IEEE Transactions on Systems, Man and Cybernetics – Part B*, vol. 37, no. 6, pp. 1512–1528, December 2007.

[20] I. L. Kurtzer, J. A. Pruszynski, and S. H. Scott, "Long-latency reflexes of the human arm reflect an internal model of limb dynamics," *Current Biology*, vol. 18, no. 6, pp. 449–453, 2008.

[21] M. W. Spong, S. Hutchinson, and M. Vidyasagar, *Robot modeling and control*. Wiley New York, 2006, vol. 3.

[22] J. Gonzalez and G. Widmann, "Investigation of non-linearities in the force control of real robots," *IEEE Transactions on Systems, Man and Cybernetics*, vol. 22, no. 5, pp. 1183–1193, Sep 1992.

[23] C. Canudas de Wit, H. Olsson, K. Aström, and P. Lischinsky, "A new model for control of systems with friction," *IEEE Transactions on automatic control*, vol. 40, no. 3, pp. 419–425, 1995.

[24] S. Huang, K. Tan, and T. Lee, "Adaptive friction compensation using neural network approximations," *IEEE Transactions on Systems, Man, and Cybernetics, Part C: Applications and Reviews*, vol. 30, no. 4, pp. 551–557, Nov 2000.

[25] M. R. Kermani, R. V. Patel, and M. Moallem, "Friction identification and compensation in robotic manipulators," *IEEE Transactions on Instrumentation and Measurement*, vol. 56, no. 6, pp. 2346–2353, 2007.

[26] A. Mohammadi, M. Tavakoli, H. Marquez, and F. Hashemzadeh, "Nonlinear disturbance observer design for robotic manipulators," *Control Engineering Practice*, vol. 21, no. 3, pp. 253 – 267, 2013.

[27] J. A. Sanford, *Universal design as a rehabilitation strategy: Design for the ages*. Springer Publishing Company, 2012.

[28] V. Mathiowetz, K. Weber, N. Kashman, and G. Volland, "Adult norms for the nine hole peg test of finger dexterity," *The Occupational Therapy Journal of Research*, vol. 5, no. 1, pp. 24–38, 1985.

[29] S. Bansil, N. Prakash, J. Kaye, S. Wrigley, C. Manata, C. Stevens-Haas, and R. Kurlan, "Movement disorders after stroke in adults: a review," *Tremor and Other Hyperkinetic Movements*, vol. 2, 2012.